Energy Reports 8 (2022) 4359–4372

Contents lists available at ScienceDirect

Energy Reports

journal homepage: www.elsevier.com/locate/egyr

Research paper

Two-level energy harvesting strategy for multi-input thermoelectric energy system

Wenchao Zhu [a,b], Xiaolong Li [a], Yang Li [a], Changjun Xie [a,b,*], Ying Shi [a]

[a] School of Automation, Wuhan University of Technology, 430070, Wuhan, China
[b] Hubei Key Laboratory of Advanced Technology for Automotive Components, Wuhan University of Technology, 430070, Wuhan, China

ARTICLE INFO

Article history:
Received 14 September 2021
Received in revised form 8 December 2021
Accepted 13 March 2022
Available online 27 March 2022

Keywords:
Automotive exhaust thermoelectric generator
Parallel thermoelectric generator
Two-level energy harvesting strategy
Fuel Economy
Over-charging

ABSTRACT

The inevitable non-uniform temperature distribution across a large number of thermoelectric modules can cause reduced output power of the automotive exhaust thermoelectric generator (AETEG). In order to achieve accurate tracking of maximum power point for an AETEG, a distributed thermoelectric energy recovery system is proposed consisting of several parallel thermoelectric generators and a lithium-ion battery pack. And then, a two-level energy harvesting strategy is developed to efficiently recover exhaust energy under dynamic driving cycles. The simulated results based on an experimentally validated system model under the modified Highway Fuel Economy Test (HWFET) for a commercial heavy-duty vehicle demonstrate that the proposed strategy enables the system to run at the efficient working point of DC/DC converters. It shows that the charging energy can be increased by 174013 J and the efficiency of system-control level can be raised by 2.4% compared to the conventional feedback control under the modified HWFET driving cycle, when the initial State of Charge (SOC) of the battery pack is 10%. Meanwhile, the proposed strategy can avoid the over-charging events for the battery pack since it can be effectively controlled along its pre-defined optimal working trajectory, which is verified by the campus road test.

1. Introduction

Energy security and environmental issues are the two major driving forces for the increasing research on automotive exhaust emission reduction. About two-thirds of the energy released from the automotive fuel is consumed as waste heat through the exhaust gas (Fernández-Yáñez et al., 2018; Jaziri et al., 2020; Kishita et al., 2016). Recovering the waste heat energy in the exhaust gas of the automotive and converting it to power for battery charging can supply additional energy to the vehicle. Automotive exhaust thermoelectric generator (AETEG) is the most promising technology for such a purpose to reuse the energy in vehicles.

Thermoelectric technology is the conversion between thermal energy and electrical energy according to the Seebeck effect and the Peltier effect of semiconductor thermoelectric materials, which provides effective ways to recover automotive exhaust waste heat (Hewawasam et al., 2020; Zhang et al., 2020). In recent years, many research efforts have been directed to the regeneration of electric power from the automotive exhaust gas using TEGs. Haidar and Ghojel (2001) designed a compact device incorporating six bismuth-telluride (BiTe) thermoelectric modules (TEMs) with the exhaust pipe as the heat source of a gasoline-engine vehicle, and the output power is 42.3 W when the hot side and the cold side temperatures are 503.15 K and 303.15 K, respectively. Elsner et al. developed and experimentally validated a 1-kW TEG for diesel trucks, using 72 BiTe TEMs rated at 14 W. Karri et al. (2011) reported a power reduction and fuel-saving scheme for a sports utility vehicle (SUV) by combining an AETEG and a stationary compressed-natural-gas-fueled engine-generator set. The TEG is comprised of the HZ20M modules, and the output powers are 33 W, 82 W, and 140 W at the vehicle speed of 48.3 km/h, 80.5 km/h, and 112.7 km/h, respectively. Crane et al. (2013) integrated a high-temperature TEG into a BMW X6 and a Lincoln MKT. The output power obtained on the test bench is over 700 W, while 600 W can be achieved from a vehicle test. Liu et al. (2015) designed a four-TEG system and it was integrated with a prototype vehicle named "Warrior". At the temperature difference of 182 K and 240 K, the maximum output powers of the system were 600 W and 944 W, from the road test and the revolving drum test, respectively. The corresponding system efficiencies in the two tests were improved by 1.28% and 1.85%, respectively. In general, it can be seen that appreciable technological and economic benefits can be reaped by using AETEG for vehicles.

Due to the limited power and voltage ratings of a single TEM based on the current technology, a large number of TEMs need to

* Corresponding author at: School of Automation, Wuhan University of Technology, 430070, Wuhan, China.
E-mail address: jackxie@whut.edu.cn (C. Xie).

https://doi.org/10.1016/j.egyr.2022.03.123

Nomenclature

α_{PN}	Seebeck coefficient(V/K)
ρ_{PN}	Electrical resistivity (Ω m)
U_{OC}	Open-circuit voltage(V)
R_{TEG}	Internal resistance(Ω)
$\eta_{con,avg}$	Average efficiency
E_{chg}	Charging energy(J)

Abbreviations

TEM	Thermoelectric module
TEG	Thermoelectric generator
AETEG	Automotive exhaust thermoelectric generator
MPPT	Maximum power point tracking
SOC	State of Charge
HWFET	Highway fuel economy test
SEPIC	Single-ended primary inductor converter
DC/DC	Direct current/Direct current
MISO	Multi-input single-output

be connected in series or/and in parallel to achieve high power and high voltage output to meet the operating requirement of the vehicle. Conventionally, in an AETEG, these TEMs are controlled in a centralized manner by assuming that all the TEMs have identical parametric characteristics and operating states. However, due to the manufacturing differences of the module and the non-uniform temperature distribution, there are inevitable inconsistencies in the performances amongst different TEMs, and this can result in problems such as power mismatch among the modules and series power losses (Yang et al., 2020). The problems can be effectively solved by adopting a distributed control framework based on a multi-string power converter. Compared to the conventional centralized architecture (Yu and Chau, 2009), there are three distinct advantages to use the distributed control scheme for the AETEG (Li et al., 2011). First, this method enables higher utilization of waste heat by considering the different properties of the TEMs at different locations. Second, the multi-string topology of the power converter increases the reliability of the whole system. Furthermore, the accurate maximum power of each subsystem can be achieved. Such a distributed architecture can be achieved by connecting the TEMs either in series or in parallel, depending on the voltage level of the interconnected system (Wu et al., 2014, 2013a). In this study, since a $LiFePO_4$ battery pack is connected with a narrow range of terminal voltage variation, the parallel connection of the TEMs is selected.

The control tasks of the proposed system, including regulation of the output voltage of the AETEG, maximum power point tracking (MPPT), and optimal battery charging, shall be achieved by using a dc/dc power converter. Many well-established step-up/down converters, such as the buck (Sun et al., 2014) and the boost converters (Twaha et al., 2017b), have been incorporated into the TEG systems. However, these traditional converters suffer from problems including low conversion gain, high device stress, and opposite input/output currents. To sidestep the issues, the converters with a high step-up gain are proposed for TEM applications. For example, in (Ashraf and Masoumi, 2016), Ashraf et al. proposed to use the boost converter with an auxiliary transformer. Nagayoshi et al. (2011) designed a practical high-efficiency thermoelectric power conditioner, using an H-bridge buck–boost switching converter which achieves both voltage step-up and step-down. Furthermore, a buck-cascaded-boost converter has been successfully applied to the TEG systems (Kim and Lai, 2008; Park et al., 2015), whereas two bulky filter inductors have to be used in this converter. Hence, this configuration decreases the power density and increases the cost and size of the converter. To overcome the drawback, Wu et al. (2013b) proposed a buck–boost converter with a coupled inductor for the TEG battery power conditioning system. Unfortunately, this converter has low current ripples and low device stress. In the present investigation, the single-ended primary inductor converter (SEPIC) (Eakburanawat and Boonyaroonate, 2006) with both high voltage step-up and step-down capabilities is for the first time employed for the AETEG application. The SEPIC has the advantages of simple structure and it is well-suited for the AETEG system with the required wide output voltage range.

Since the vehicle engine is always operating under variable working conditions, to increase the energy conversion efficiency, it is necessary to track the maximum output power of the AETEG delivered to the varying load. Various MPPT algorithms have been proposed for the applications of renewable generation systems such as solar photovoltaic (PV) (Ali et al., 2020; Liu and Liu, 2020; Mao et al., 2020; Yang et al., 2019). As a TEG system shares a similar power vs. voltage characteristic with a PV system, most MPPT algorithms for the PV systems can be applied to the AETEG systems with minor modifications. Montecucco and Knox (2015) and Park et al. (2014) used the open-circuit voltage (OCV) characteristics of the TEG to generate proper reference voltage signals. In their works, the experimental maximum power tracking errors are 0.15% and 1.15%, respectively. Perturb and observation (P&O) method (Dalala et al., 2018) and hill-climbing method (Carstens and Gühmann, 2015) are also widely applied for TEG systems. In order to achieve the maximum power generation rapidly and accurately, Liu et al. (2016) proposed a hybrid MPPT algorithm combining the P&O and the OCV methods, while Fang et al. (2016) introduced the combination of the dichotomy and the gradient methods. Twaha et al. (2017a) presented the extremum seeking control method to realize the MPPT for the TEG systems. Compared to the P&O method, the extremum-seeking control method can extract 0.47 W or 6.1% more power when the hot-side temperature is 473.15 K. To further increase the energy production of the AETEG and balance the power flows of the proposed system, an effective energy management strategy is also essential. Kim and Lai (2008) proposed a seamless mode transfer MPPT controller, including the MPPT mode and power balance mode. Wu et al. (2013b) employed a control method to ensure smooth switching among different working modes. The general problems in the above schemes are that they do not consider the power losses of the dc/dc converters, and the centralized MPPT algorithms are not optimal for all TEMs with distributed characteristics.

In this paper, to solve the identified problems, a two-level energy harvesting strategy is thereby developed to guarantee the optimized operation of the AETEG system considering the uneven losses of the multi-string SEPIC dc/dc converter. The proposed control architecture consists of two levels including the device-level control and the system-level control. First, at the device level, the AETEG works in two modes, i.e., the MPPT mode and the constant current mode. In the meanwhile, the battery is controlled by using a droop method, so that the AETEG and the battery can work at the MPPT and the optimal charging state, respectively. On the other hand, at the system level, the proposed energy harvesting strategy incorporates an equivalent generation maximizing algorithm to minimize the power loss of multi-string dc/dc converters, and the formulated optimization problem is solved by dynamic programming (DP).

The main contributions and innovations of this paper can be summarized as follows.

(1) A polygonal AETEG with eighteen sides is created and divided into high-temperature, medium-temperature, and low-temperature zones. To form a distributed thermoelectric energy recovery system, three strings of MISO (Multi-input single-output) parallel converters are used to connect the high-temperature, medium-temperature, and low-temperature regions to the $LiFePO_4$ battery pack.

(2) A two-stage energy control strategy is proposed. To control the AETEG and the $LiFePO_4$ battery pack, the MPPT/constant current mode and the sag method are used as device control stages. As the system control stage, an energy harvesting strategy based on a hybrid algorithm of EGMS and DP is used to optimize overall power loss.

(3) A modified HWFET driving cycle is designed, a dynamic model of the system is created, and the proposed energy harvesting strategy's performance is evaluated through simulation. The entire vehicle experimental platform is developed, and campus road tests are designed to evaluate the thermoelectric energy recovery system's overall performance.

The rest of the paper is organized as follows. The model of the proposed distributed thermoelectric energy recovery system is presented in Section 2. The characteristics and the efficiency of the dc/dc converter and the optimal charging power of the battery are described in Section 3. The two-level energy harvesting control scheme is proposed in Section 4. In Section 5, simulations under different working conditions and campus road tests are provided to validate the proposed method. Finally, conclusions are given in Section 6.

2. System configuration and modeling

As mentioned in the introduction, an AETEG usually includes many TEMs with different characteristics. Non-uniform temperature distribution exists across the TEMs as their physical distances to the heat exchanger and the cooling system are different. This inconsistency in the performance of TEMs can lead to a reduction of the practical output power of the AETEG.

The TEG used in the present study is divided into several segments, and each segment is connected to a distributed power conditioner. The power conditioner can ensure that each segment is operating in the corresponding MPPT mode. In this study, a distributed thermoelectric energy recovery system is proposed and its schematic diagram is shown in Fig. 1. The example system consists of a TEG and a 51.2-V 60-Ah lithium-iron-phosphate ($LiFePO_4$) battery pack, designed for a heavy-duty commercial vehicle (Li et al., 2018). The TEG and the battery pack are connected via a three-string parallel-connected multi-input single-output (MISO) dc/dc converter consisting of three SEPIC structures. The specification of the system is given in Table 1. In the proposed system, the output power of the TEG and the current of the battery pack are coordinately controlled by manipulating the three SEPIC dc/dc units in the MISO converter. By this means, accurate MPPT can be achieved for each segment of the TEG. The mathematical model of the proposed system will be presented next.

2.1. Modeling of automotive exhaust thermoelectric generator

As shown in Fig. 2(a), the presented TEG is a cylinder-shaped device, i.e., its cross-section is an eighteen-sided polygon. The side length of the eighteen-sided polygon and the height of the prism are 80 mm and 1000 mm, respectively. The TEG consists of 306 TEMs which can be divided into three segments based on their distances to the heat exchanger and the cooler: the high-temperature region, the medium-temperature region, and the low-temperature region. As shown in Fig. 2(b), the TEMs are divided into 17 rows in the streamwise direction and 18 columns located in the plane perpendicular to the heat flow. From the direction of exhaust inlet, the TEMs between the 1st and the 7th rows belong to the high-temperature region, the 8th to the 12th rows are located in the medium-temperature region, while the 13th to the 17th rows are in the low-temperature region. Furthermore, Fig. 2(c) illustrates the equivalent circuit of each segment of the TEG, and the 18 TEMs distributed in the same row of the TEG connect first in parallel and then in series to the next row. The specifications of each TEM are listed in Table 2.

Table 1
Parameters of the proposed system.

Subsystem	Description	Value
TEG	Maximum power (W)	1500
	Maximum open-circuit voltage (V)	350
	Voltage of maximum power (V)	177
	Current of maximum power (A)	8.47
	Maximum temperature difference (K)	250
Battery pack	Rated voltage (V)	51.2
	Rated capacity (A h)	60
Engine	Displacement (L)	11.12
	Rated power (kW)	303
	Maximum torque (N m)	2000
DC/DC#1	Input voltage (V)	40–150
	Output voltage (V)	40–60
	Output current (A)	0–20
	Rated power (W)	1200
DC/DC#2	Input voltage (V)	20–100
	Output voltage (V)	40–60
	Output current (A)	0–10
	Rated power (W)	600
DC/DC#3	Input voltage (V)	10–70
	Output voltage (V)	40–60
	Output current (A)	0–8.33
	Rated power (W)	500

Table 2
Specifications of the TEM.

Parameter	Value
Dimensions (L · W · H, mm)	50 × 50×4.2
Weight (g)	47
Maximum power (W)	14.0
Hot/Cold-side temperature (K)	523.15/303.15
Conversion efficiency (%)	5.6
Number	304
Material	Bi_2Te_3
Manufacturer	Guangdong Fuxin

The AETEG model is developed and verified using our bench test data. Denote i the index of the row ($i \in 1, 2, \ldots, 17$), the OCV U_{OC-H}, the internal resistances R_{TEG-H}, and the maximum output power P_{MAX-H} of high-temperature region of the AETEG are expressed as (Li et al., 2018):

$$U_{OC-H} = \sum_{i=1}^{7} N \cdot \alpha_{PNi} \cdot \Delta T_i \tag{1}$$

$$R_{TEG-H} = \sum_{i=1}^{7} (N/18) \cdot \rho_{PNi} \cdot (L/S) \tag{2}$$

$$P_{MAX-H} = U_{OC-H}^2 / (4R_{TEG-H}) \tag{3}$$

where N is the number of PN junctions in each TEM, ΔT_i is the temperature difference between the hot sides and the cold sides of TEMs, L is the length of the thermoelements, and S is the cross section area of one pair of PN junctions. Here, the Seebeck coefficient α_{PNi} and the electrical resistivity ρ_{PNi} of thermoelectric material of the TEMs are given by Li et al. (2018):

$$\alpha_{PNi} = \left(22224 + 930.6 \cdot T_{mi} - 0.9905 \cdot T_{mi}^2\right) \times 10^{-9} \tag{4}$$

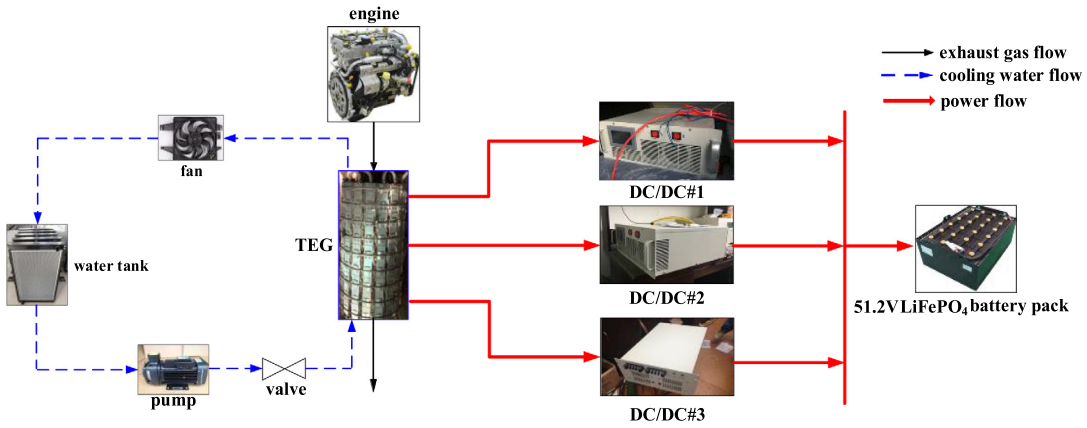

Fig. 1. Schematics of the distributed thermoelectric energy recovery system.

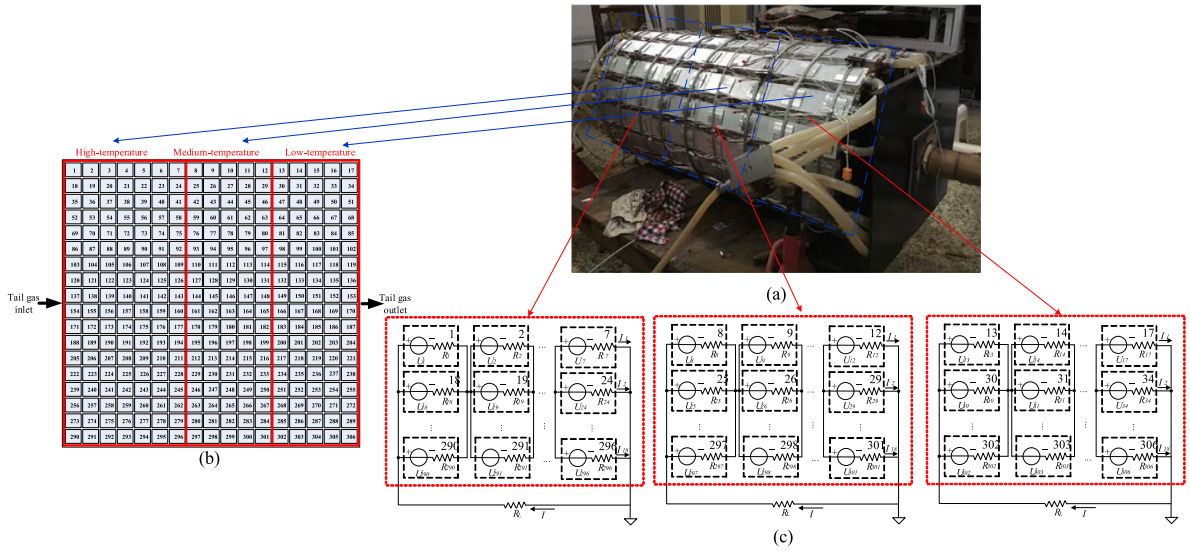

Fig. 2. (a) TEG structure for Tianlong; (b) Number of TEMs in the high-temperature, the medium-temperature, and the low-temperature regions; (c) Equivalent circuit of each segment of TEG.

$$\rho_{PNi} = \left(5112 + 163.4 \cdot T_{mi} + 0.6279 \cdot T_{mi}^2\right) \times 10^{-10} \tag{5}$$

where T_{mi} represents half of ΔT_i. Similarly, for the medium- and the low-temperature regions, the corresponding OCVs, the internal resistances, and the maximum output powers are

$$U_{OC-M} = \sum_{i=8}^{12} N \cdot \alpha_{PNi} \cdot \Delta T_i \tag{6}$$

$$R_{TEG-M} = \sum_{i=8}^{12} (N/18) \cdot \rho_{PNi} \cdot (L/S) \tag{7}$$

$$P_{MAX-M} = U_{OC-M}^2 / (4R_{TEG-M}) \tag{8}$$

$$U_{OC-L} = \sum_{i=13}^{17} N \cdot \alpha_{PNi} \cdot \Delta T_i \tag{9}$$

$$R_{TEG-L} = \sum_{i=13}^{17} (N/18) \cdot \rho_{PNi} \cdot (L/S) \tag{10}$$

$$P_{MAX-L} = U_{OC-L}^2 / (4R_{TEG-L}) \tag{11}$$

In order to validate the AETEG model, the engine were tested under five typical operating conditions as given in Table 3. The maximum output power of the high-, medium-, and low-temperature regions obtained from the presented AETEG model and from the bench test are compared in Fig. 3. The result validates that the proposed model is capable of accurately predicting the engine power with the maximum absolute error of only 3.6%.

Table 3
Five typical operating conditions of the engine.

Condition	(i)	(ii)	(iii)	(iv)	(v)
Speed (RPM)	1000	1500	2500	3500	4500
Torque (Nm)	270	500	500	461	360

2.2. Battery pack model

In order to reuse the automotive exhaust thermoelectric energy, a $LiFePO_4$ battery pack is utilized as the on-vehicle energy storage. The battery pack consists of 16 battery cells connected in series. The transient of the battery is ignored in this study for the sake of simplicity. Hence, the battery dynamics can be described by

$$SOC(t) = SOC_{t0} - \frac{1}{Q_b} \int_{t0}^{t} I_{bat}(t)\, dt \tag{12}$$

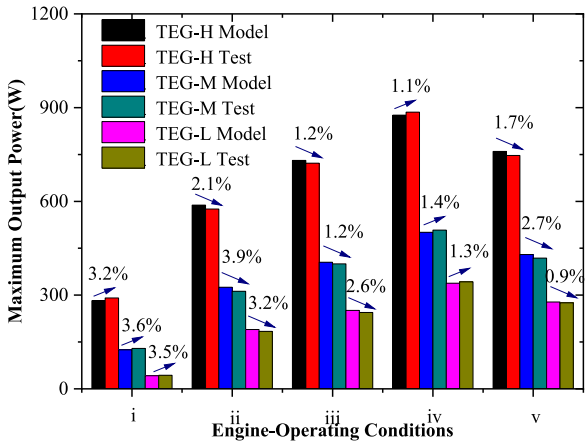

Fig. 3. Comparison of maximum output power between proposed model and bench test results.

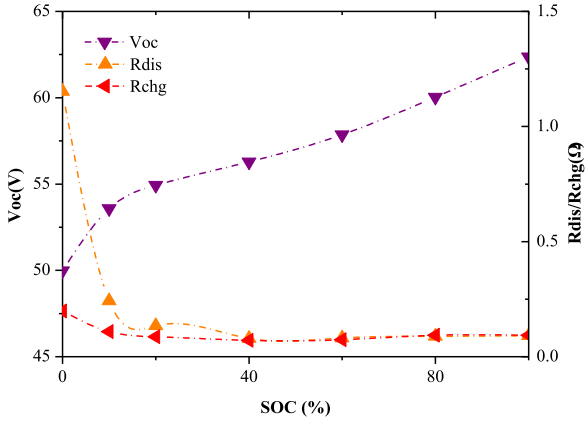

Fig. 4. Relationships between the open-circuit voltage, internal charge/discharge resistances and the state of charge the $LiFePO_4$ battery pack.

$$I_{\text{bat}}(t) = \frac{V_{\text{oc}}(t) - \sqrt{V_{\text{oc}}^2(t) - 4R_{\text{int}} \cdot P_{\text{bat}}(t)}}{2R_{\text{int}}} \tag{13}$$

where SOC_{t0} is the initial SOC at time t_0. V_{oc}, R_{int}, P_{bat}, I_{bat}, and Q_b are the OCV, internal resistance, output power, output current, and the capacity of the battery pack, respectively (Li et al., 2018). The OCV and the internal resistance are expressed as functions of the SOC as shown in Fig. 4. In Fig. 4, R_{int} is R_{dis} for the discharging process, while being R_{chg} for the charging process. Here, the internal resistance of the battery is assumed not affected by the temperature change and battery degradation for simplicity.

2.3. General model for the parallel-connected multi-input single-output DC/DC converter

As mentioned earlier, in order to increase the output power and the voltage level of the AETEG, and to achieve high system reliability with redundant power supply, a three-string MISO parallel converter is used to connect the high-, medium-, and low-temperature regions to the battery pack, and each string is a conventional SEPIC dc/dc converter. Fig. 5 shows the equivalent circuit model of the converter, which is composed of the three voltage sources E_H, E_M, and E_L, as well as three internal impedances R_H, R_M, and R_L. It is assumed that the converter gain is unity and the equivalent lumped impedances of the three strings are denoted by Z_1, Z_2, and Z_3, respectively. According to the power

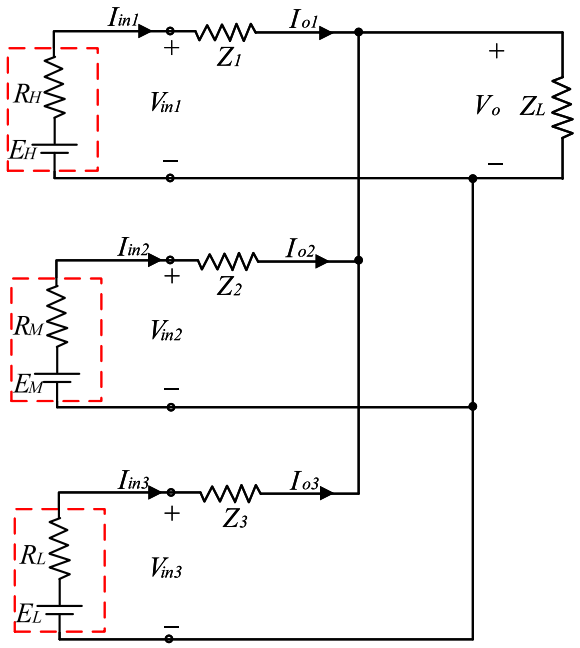

Fig. 5. Equivalent circuit of the multi-input single-output parallel dc/dc converters.

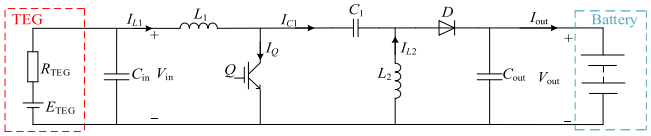

Fig. 6. Topological structure of SEPIC dc/dc converter.

balance relationships, we have

$$V_{\text{in1}} \cdot I_{\text{in1}} \cdot \eta_1 = V_{\text{o}} \cdot I_{\text{o1}} \tag{14}$$

$$V_{\text{in2}} \cdot I_{\text{in2}} \cdot \eta_2 = V_{\text{o}} \cdot I_{\text{o2}} \tag{15}$$

$$V_{\text{in3}} \cdot I_{\text{in3}} \cdot \eta_3 = V_{\text{o}} \cdot I_{\text{o3}} \tag{16}$$

where V_{in1}, V_{in2}, and V_{in3} are the output voltages of the high-, medium-, and low-regions of the AETEG. Similarly, for the SEPIC converters for the three regions of the AETEG, I_{in1}, I_{in2}, and I_{in3} are corresponding the output currents, η_1, η_2, and η_3 are the conversion efficiencies, and I_{o1}, I_{o2}, and I_{o3} are the output currents, while V_o is the common output voltage of the converter which is equal to the voltage of the load impedance. The detailed configuration of the SEPIC unit is shown in Fig. 6. The converter is established to cope with the power mismatch in the AETEG. As mentioned in the previous section, the wide output voltage range and simple topology with only one switching device make the control of the multi-string converter simple.

3. Analysis of the DC/DC conversion efficiency

Fig. 7 shows the equivalent circuit topology for the analysis of the power loss of the SEPIC converter based on the circuit shown in Fig. 6. In Fig. 7, V_{in} is the input voltage, R_{on} is the on-state resistance of the power device, V_{on} is the diode-on voltage drop, R_{L1} and I_{L1} are the equivalent resistance and average current of the inductor L_1, and R_{L2} and I_{L2} are the equivalent resistance and the average current of the inductor L_2. R_{C1} and R_{Cout} are the equivalent series resistances of capacitor C_1 and C_{out}, respectively.

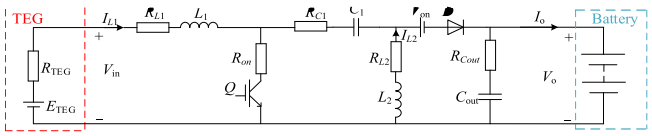

Fig. 7. Equivalent circuit of the SEPIC converter for power loss analysis.

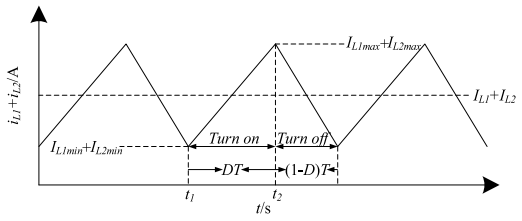

Fig. 8. The sketch of the inductor current.

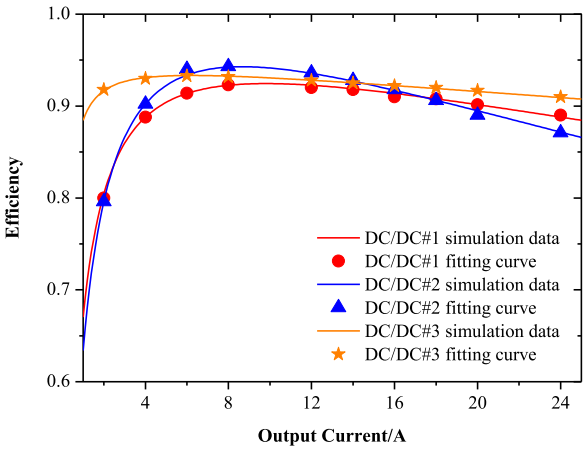

Fig. 9. Efficiency curves of three SEPIC converters.

I_o and V_o are the output current and the output voltage, respectively. The efficiency of the converter is defined and calculated by

$$\eta = \frac{P_{\text{out}}}{P_{\text{in}}} = \frac{P_{\text{out}}}{P_{\text{out}} + P_{\text{switch}} + P_{\text{conduction}}} \tag{17}$$

where, P_{in} is the input power, $P_{\text{out}} = V_o I_o$ is the output power, P_{switch} is the switching loss of the power device, and the conduction loss $P_{\text{conduction}}$ includes the voltage drop loss of the diode and the loss of various resistors.

The switching loss of the power device P_{switch} depends on the voltage and the current during switching, the turn-on time, the turn-off time, and the switching frequency. P_{switch} is calculated by (Nagayoshi et al., 2011):

$$P_{\text{switch}} = \frac{V_{\text{in}} + V_{\text{o}}}{2} \cdot I_{\text{m1}} \cdot t_{\text{on}} \cdot \text{f} + \frac{V_{\text{in}} + V_{\text{o}}}{2} \cdot I_{\text{m2}} \cdot t_{\text{off}} \cdot \text{f} \tag{18}$$

where f is the switching frequency, I_{m1} is the maximum operating current when the device is turned on, t_{on} is the turn-on time, I_{m2} is the maximum operating current when the device is turned off, and t_{off} is the turn-off time.

The demonstrative waveform of the inductor current of the converter is illustrated in Fig. 8. Here D is the on-duty ratio of the switch, T is the switching period, I_{L1} and I_{L2} are the average currents of the inductors L_1 and L_2, respectively. $I_{L1\max}$ and $I_{L1\max}$ are the peak and the valley of the inductor current of L_1, and while $I_{L2\max}$ and $I_{L2\min}$ are the peak and the valley of the inductor current of L_2 respectively.

As shown in Fig. 8, suppose at time point t_1, the power device is turned on, and the device current rises. At the end of the turn-on process, $I_{m1} = I_{L1\max} + I_{L2\min}$, and the turn-on loss is $(V_{\text{in}} + V_o) \cdot (I_{L1\max} + I_{L2\min}) \cdot t_{\text{on}} \cdot f/2$. At t_2, the power device is turned off, and the device current drops. At the end of turn-on process, $I_{m2} = I_{L1\max} + I_{L2\max}$, and the turn-off loss is $(V_{\text{in}} + V_o) \cdot (I_{L1\max} + I_{L2\max}) \cdot t_{\text{off}} \cdot f/2$.

According to the peak-to-peak value and the ripple of the current in Fig. 8, the maximum operating currents when the device is in the on- and the off-states are calculated as (Montecucco and Knox, 2015):

$$I_{\text{m1}} = I_{L1} + I_{L2} - \left(\frac{V_{\text{in}}}{2L_1} + \frac{V_{\text{in}}}{2L_2}\right) \cdot \text{DT} \tag{19}$$

$$I_{\text{m2}} = I_{L1} + I_{L2} + \left(\frac{V_{\text{o}}}{2L_1} + \frac{V_{\text{o}}}{2L_2}\right) \cdot (1 - \text{D})\, T \tag{20}$$

Therefore, the switching loss of the power device is calculated as

$$P_{\text{switch}} = \frac{V_{\text{in}} + V_{\text{o}}}{2} \cdot \text{f} \cdot (I_{L1} + I_{L2}) \cdot (t_{\text{on}} + t_{\text{off}}) + \frac{(V_{\text{in}} + V_{\text{o}})\,(L_1 + L_2)}{4L_1L_2} \cdot [V_{\text{o}} \cdot (1 - \text{D})\, t_{\text{off}} - V_{\text{in}} \cdot \text{Dt}_{\text{on}}] \tag{21}$$

Next, the conduction loss $P_{\text{conduction}}$ consists of the power device on-state loss $(I_{L1} + I_{L2})^2 DR_{\text{on}}$, the diode dropout loss $(I_{L1} + I_{L2})(1\text{-}D)V_{\text{on}}$, the inductor equivalent loss $(I_{L1}^2 R_{L1} + I_{L2}^2 R_{L2})$, and the capacitor equivalent loss $(I_o^2 DR_{\text{Cout}} + I_{L2}^2 DR_{C1} + (I_{L1} + I_{L2} - I_o)^2 (1\text{-}D)R_{\text{Cout}})$.

According to the working principles of the SEPIC converter, the currents of inductors L_1 and L_2 are expressed as

$$\begin{cases} I_{L1} = \frac{\text{D}}{1-\text{D}} \cdot I_{\text{o}} \\ I_{L2} = \frac{2-\text{D}}{1-\text{D}} \cdot I_{\text{o}} \end{cases} \tag{22}$$

Substituting (21) and (22) into (17), the efficiency the SEPIC converter can be expressed as a function of the output voltage and output current, i.e.,

$$\eta = \frac{V_{\text{o}} I_{\text{o}}}{\text{c}_1 I_{\text{o}}^2 + \text{c}_2 I_{\text{o}} + \text{c}_3} \tag{23}$$

where

$$\text{c}_1 = \frac{4DR_{\text{on}} + \text{D}^2 R_{L1} + (2 - \text{D})^2 R_{L2} + (2 - \text{D})^2 DR_{C1} - (\text{D}^3 + \text{D}^2 - 2\text{D} - 1) R_{\text{Cout}}}{(1 - \text{D})^2}$$

$$\text{c}_2 = V_{\text{o}} + \frac{V_{\text{in}} + V_{\text{o}}}{1 - \text{D}} \cdot \text{f} \cdot (t_{\text{on}} + t_{\text{off}}) + 2V_{\text{on}}$$

$$\text{c}_3 = \frac{(V_{\text{in}} + V_{\text{o}})\,(L_1 + L_2)}{4L_1L_2} \cdot [V_{\text{o}}\,(1 - \text{D})\, t_{\text{off}} - V_{\text{in}} \text{D} t_{\text{on}}]$$

Here, the coefficients c_1, c_2, and c_3 are determined by the operating parameters, the line parasitic parameters, and the component parameters. Since the parasitic parameters of the converter and some practical operating parameters of the components cannot be measured accurately in practice, c_1, c_2, and c_3 shall be determined based on the sample data of the converter.

The simulation conditions of the SEPIC units 1, 2, and 3 are described in Table 4. According to SEPIC converter circuit simulation data and results from the MATLAB curve fitting tool, the fitted functional relationships between the efficiency and the current of three SEPIC converters are obtained and compared in Fig. 9. Since the sum of squared errors of data points in converter 1, 2, 3 is 0.0008767, 0.003651, and 0.0001194, respectively, the efficiency curve fitted by the efficiency function (24) is approximately close to the simulation data.

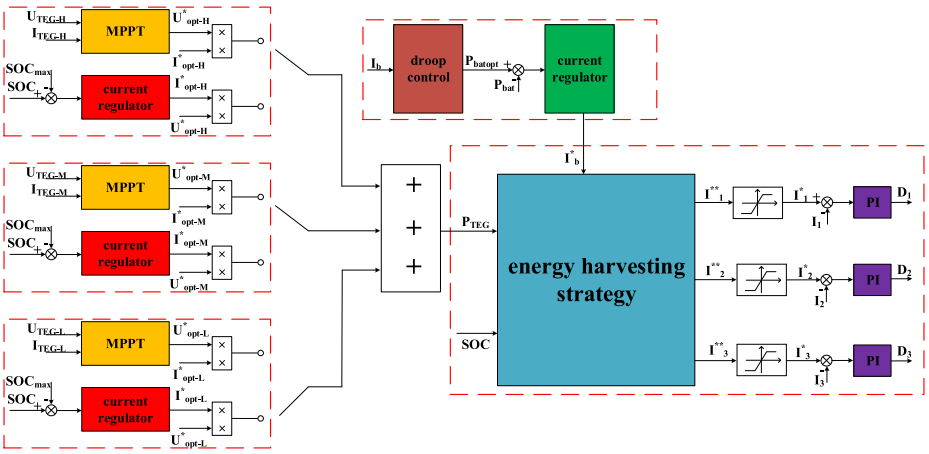

Fig. 10. Control architecture of the proposed automotive exhaust thermoelectric generator energy recovery system.

Table 4
Simulation conditions of sepic circuits.

Sepic circuit	1	2	3
Input voltage (V)	120	100	60
Output voltage (V)	48	48	48
Power device on-resistance (Ω)	0.042	0.04	0.035
Diode voltage drop (V)	0.7	0.7	0.7
Inductance L_1/L_2 (mH)	0.5	0.35	0.2
Inductance equivalent resistance (Ω)	0.08	0.047	0.019
Capacitance C_1/C_2 (mF)	1	1	1
Capacitor equivalent resistance (Ω)	0.01	0.01	0.01
Switching frequency (kHz)	20	20	20

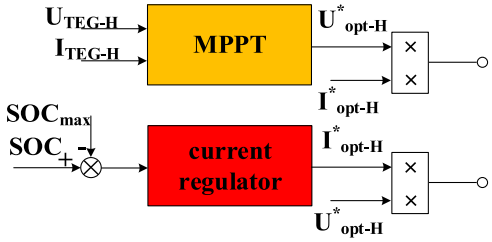

Fig. 11. Block diagram of control system for the high-temperature region of the automotive exhaust thermoelectric generator.

4. Two-level energy harvesting strategy

4.1. Control objectives

The primary goal of the control strategy is to recover the automotive exhaust waste heat as much as possible in the meanwhile to minimize the power converter loss in the presence of the unbalanced temperature distribution in AETEG. In addition, the proposed strategy should be able to consider battery health. In this study, the energy harvesting strategy is to achieve the following specific control objectives:

(1) To ensure that the AETEG works at the MPPT mode;
(2) To minimize the dc/dc converter loss and increase the system efficiency;
(3) To maintain the SOC of the battery pack within an efficient region and avoid over-charge/over-discharge;
(4) To enhance the battery life by keeping the battery pack working at the optimal point as much as possible.

In this study, a two-level energy harvesting strategy is proposed to achieve the above control objectives. The block diagram of the control architecture of the AETEG system is shown in Fig. 10. At the device control level, the AETEG and battery pack are controlled by different control methods to realize the reasonable power distribution and stable operation of the system. Specifically, the AETEG works in two operating modes under different operating states, while the battery pack is regulated by droop control to obtain the optimal power of battery pack. At the system control level, the generation power of the AETEG is distributed by the MISO parallel converter with three SEPIC units to minimize the dc/dc converter loss, based on a hybrid algorithm consisting of the equivalent generation maximizing strategy (EGMS) and DP.

4.2. Device control level

4.2.1. Automotive exhaust thermoelectric generator control

In this system, the AETEG supplies power to the battery pack by three SEPIC converters. The AETEG has two working modes under different operating states: the MPPT mode and the current mode. The AETEG works mostly in the MPPT mode to recycle waste heat energy as much as possible. However, it will be switched to the current mode when the SOC of battery pack is close to its upper limit SOC_{max}, or when its output power is higher than the power rating. The control architecture for the high-temperature region AETEG is shown in Fig. 11, while the medium-temperature region and low-temperature region of the AETEG share a similar control structure.

4.2.2. Battery pack control

The battery pack plays an important role in storing the waste heat recovery energy and in stabilizing the vehicle electrical system voltage. In this study, the droop control is used to calculate the optimal power demand of the battery pack and to maintain the SOC within a suitable operating range. The block diagram of droop control is shown in Fig. 12, it can be expressed as

$$P_{\text{batopt}} = P_{\text{H}} - \text{m}I_b \quad I_b < 0, \text{charging} \tag{24}$$

where P_{batopt} is the optimal power demand of battery pack, P_H is the critical power value of charging, I_b is the output current of battery pack, and m is the adaptive droop coefficient.

The adaptive droop coefficient m is determined by battery SOC, which can be expressed as

$$\text{m} = \text{m}^*\text{SOC} \quad I_b < 0, \text{charging} \tag{25}$$

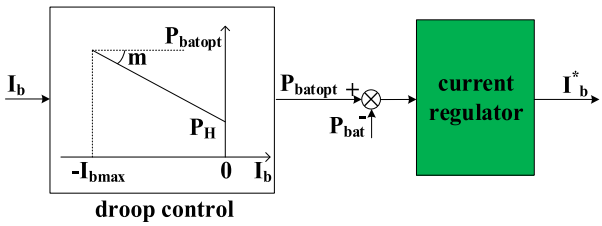

Fig. 12. Block diagram of the battery pack control system.

where the initial droop coefficient m^* is calculated as

$$\mathrm{m}^* = \frac{\Delta P}{I_{\mathrm{bmax}}} \tag{26}$$

where, ΔP is the maximum power fluctuation range, I_{bmax} is the maximum charging current.

In the charging process, the droop coefficient m increases with the increase of SOC, and the charging current gradually decreases.

4.3. System control level

In the proposed two-level energy harvesting strategy, the energy harvesting strategy based on a hybrid algorithm consisting of EGMS and DP is considered as the system control level. As mentioned earlier, the major purpose of the proposed energy harvesting strategy is to minimize the dc/dc converter loss. Meanwhile, the proposed energy harvesting strategy can recover waste heat energy as much as possible and keep the battery pack working at the optimal point. Therefore, the proposed energy harvesting strategy should be able to improve the efficiency of the AETEG energy recovery system and extend the lifetime of battery.

4.3.1. Equivalent generation maximizing strategy

EGMS is an instantaneously optimized approach that can maximize the charging power of battery. Furthermore, the proposed EGMS can maintain the SOC of the battery pack within an efficient region. In order to maximize the charging power of battery, the AETEG is in the MPPT mode to recycle waste heat energy as much as possible. And the maximizing problem of the charging power can be formulated as

$$\begin{aligned} J_1 &= \operatorname{argmax} \sum_{\mathrm{j}=1}^{3} P_{\mathrm{TEG-j}} \cdot \eta_{\mathrm{j}} \\ \text{s.}t.\ &\begin{cases} \mathrm{SOC}_{\mathrm{min}} \le \mathrm{SOC} \le \mathrm{SOC}_{\mathrm{nom}} \\ I_{\mathrm{ojmin}} \le I_{\mathrm{oj}} \le I_{\mathrm{ojmax}} \\ P_{\mathrm{TEGmax}} = P_{\mathrm{bat}} + P_{\mathrm{loss}} \end{cases} \end{aligned} \tag{27}$$

where $j \in 1, 2, 3$ is the index of the SEPIC converter for the AETEG high-, medium-, and low-temperature region, respectively. $P_{\mathrm{TEG}-j}$ is the maximum output power and η_j is the efficiency of SEPIC converter. The optimization problem (27) is subject to several constraints. Here, $\mathrm{SOC}_{\mathrm{min}}$ and $\mathrm{SOC}_{\mathrm{nom}}$ are the lower limits of the battery SOC and upper threshold of battery SOC in the normal level; I_{ojmin} and I_{ojmax} are the minimum output current and maximum output current of the jth SEPIC converter; P_{TEGmax}, P_{bat}, and P_{loss} are the maximum output power of the AETEG, charging power of the battery pack, and the total loss power of three SEPIC converters.

As the AETEG is divided into three regions, they can be controlled by different MPPT regulators to recover the waste heat energy. This helps to improve the efficiency of the system, because the EGMS minimizes the loss of dc/dc converters during each control period. The output current references I_{o1}^*, I_{o2}^*, I_{o3}^* of DC/DC#1, DC/DC#2, DC/DC#3 are obtained via the EGMS proposed in this paper.

4.3.2. Dynamic programming

In order to improve the recovery efficiency while keeping the battery pack working at the optimal point, the DP is used in this study. DP is a global optimized method that can transform multi-stage decision problems into single-stage decision problems; therefore it can be used for global optimization problems of complex nonlinear systems with constraints. The control goal of this strategy is to minimize the dc/dc converter loss and to ensure the battery pack works at the optimal charging point as much as possible. In the proposed distributed thermoelectric energy recovery system, the current SOC of the battery pack is directly related to the output current of the jth SEPIC converter and the SOC of the previous moment. Since the efficiency of the power system is determined by the output current of the jth SEPIC converter directly, it can describe the pros and cons of the decision and it is selected as the system objective function. The change of the battery SOC describes the dynamic process of the battery, therefore, the battery SOC is selected as the state variable of the system. Because the output current of the jth SEPIC converter is related to each other, they are selected as decision variables.

As is analyzed above, the state transition equation of the distributed thermoelectric energy recovery system at time k is expressed as

$$\begin{cases} \mathrm{SOC}\,(k+1) = \mathrm{SOC}\,(k) - \frac{1}{Q_b} \cdot \left(I_{\mathrm{o1}}\,(k) + I_{\mathrm{o2}}\,(k) + I_{\mathrm{o3}}\,(k)\right) \cdot \Delta t \\ \mathrm{SOC}\,(0) = \mathrm{SOC}_0 \end{cases} \tag{28}$$

The power system consists of three SEPIC converters of different power levels connected in parallel. And the input power of the jth converter is expressed as

$$P_{\mathrm{inj}} = \frac{U_{\mathrm{o}} \cdot I_{\mathrm{oj}}}{\eta_{\mathrm{j}}} \tag{29}$$

where, U_o is the output voltage of the parallel power system, I_{oj} and P_{inj} are the output current and input power of the jth SEPIC converter. Therefore, the operating efficiency of the whole power system is expressed as

$$\eta = \frac{U_{\mathrm{o}} \cdot I_b^*}{\sum_{\mathrm{j}=1}^{3} P_{\mathrm{inj}}} = \frac{U_{\mathrm{o}} \cdot I_b^*}{\sum_{\mathrm{j}=1}^{3} \frac{U_{\mathrm{o}} \cdot I_{\mathrm{oj}}}{\eta_{\mathrm{j}}}} = \frac{I_b^*}{\sum_{\mathrm{j}=1}^{3} \frac{I_{\mathrm{oj}}}{\eta_{\mathrm{j}}}} \tag{30}$$

where, I_b^* is the charging current reference of the battery pack.

From (30), the operating efficiency of the parallel power system can be optimized by minimizing $\sum_{\mathrm{j}=1}^{3} I_{\mathrm{oj}}/\eta_{\mathrm{j}}$. The stage objective function of the operating efficiency of the parallel power system is denoted by

$$F_k\left(\mathrm{SOC}\,(k)\ I_{\mathrm{o1}}\,(k)\ I_{\mathrm{o2}}\,(k)\, I_{\mathrm{o3}}\,(k)\right) = \sum_{\mathrm{j}=1}^{3} \frac{\mathrm{c}_{1\mathrm{j}} I_{\mathrm{oj}}^2\,(k) + \mathrm{c}_{2\mathrm{j}} I_{\mathrm{oj}}\,(k) + \mathrm{c}_{3\mathrm{j}}}{U_{\mathrm{o}}} \tag{31}$$

where, c_{1j}, c_{2j}, and c_{3j} are the coefficients determined by the jth SEPIC converter operating parameters. The goal of the whole process is to minimize the sum of the objective function of each stage. And the objective function of DP is expressed as

$$J_2 = \min \sum_{k=1}^{N} F_k\left(\mathrm{SOC}\,(k)\ I_{\mathrm{o1}}\,(k)\ I_{\mathrm{o2}}\,(k)\, I_{\mathrm{o3}}\,(k)\right) \tag{32}$$

where, N is the number of stages where the whole process is divided. In order to keep the battery pack working at the optimal

point and extend the life time of battery, there is an extra constraint which ensures that the battery pack works at the optimal charging power. The constraints of energy harvesting strategy based on DP is expressed as

$$\begin{cases} \mathrm{SOC_{nom}} < \mathrm{SOC}\,(k) \le \mathrm{SOC_{max}} \\ \frac{\mathrm{dSOC}}{\mathrm{dt}} \le \Delta\mathrm{SOC} \\ I_{\mathrm{ojmin}}\,(k) \le I_{\mathrm{oj}}\,(k) \le I_{\mathrm{ojmax}}\,(k) \\ P_{\mathrm{TEG}}\,(k) = P_{\mathrm{batopt}}\,(k) + P_{\mathrm{loss}}\,(k) \\ \sum_{\mathrm{j}=1}^{3} I_{\mathrm{oj}}\,(k) = I_b^*\,(k) \end{cases} \tag{33}$$

where $\mathrm{SOC_{min}}$ and $\mathrm{SOC_{max}}$ are the lower and the upper limits of the battery SOC, respectively, ΔSOC is the maximum SOC increasing rate of the battery pack, and P_{TEG} is the output power of the AETEG.

The DP is to solve the optimization problem reversely and then to optimize positively. The specific algorithm for DP is described as follows

Step 1: Given the entire driving cycle, divide the entire time horizon into N stages;

Step 2: Evaluate the objective function when each SOC state value is converted from stage N-1 to stage N. The change path of the minimizing objective function $J_{N-1}^*\,(\mathrm{SOC}\,(N-1)) = \min F_{N-1}\,(\mathrm{SOC}\,(k)\ I_{\mathrm{o1}}\,(k)\ I_{\mathrm{o2}}\,(k)\ I_{\mathrm{o3}}\,(k))$ is taken as the actual change path. Generate an optimal distribution sequence for the output current of the jth SEPIC converter at stage N-1;

Step 3: Repeat process *Step 2* from stage $k = N$-2 to stage $k = 1$ according to

$$\mathrm{SOC}\,(k+1) = \mathrm{SOC}\,(k) - \frac{1}{Q_b} \cdot (I_{\mathrm{o1}}\,(k) + I_{\mathrm{o2}}\,(k) + I_{\mathrm{o3}}\,(k)) \cdot \Delta t$$

Step 4: Obtain an optimal path corresponding to each SOC state value until $k = 1$;

Step 5: Select a path that meets the requirements as the SOC curve, and extract the current distribution corresponding to each SOC state point.

5. Results and discussion

5.1. Device-level control discussion

In this section, the proposed energy harvesting strategy combined with the AETEG energy recovery system presented in Section 2 is verified via simulation. To confirm and compare the proposed MPPT architecture, the proposed MPPT architecture is compared with a conventional single SEPIC converter with MPPT technique under the same conditions (sampling time and PWM frequency). The studied system is tested under fast change of exhaust inlet temperature and mass flow as shown in Fig. 13.

Fig. 14(a), (b) show AETEG voltage response corresponding to conventional single SEPIC converter with MPPT technique and proposed MPPT architecture. Initially, the exhaust inlet temperature and mass flow are set to 745 K, 32.5 g/s, respectively. The ATEG voltage fluctuates around the reference voltage 642.75 V between 640.64 and 650.39 V, whereas for the proposed MPPT architecture, the AETEG voltage tracks more accurately. Next, at instant t=0.3 s, a step change of inlet temperature from 745 K to 490 K, and inlet mass flow from 32.5 g/s to 47.5 g/s is done. As shown in the enlarged part of Fig. 14(b), the voltage curve shows a fluctuating upward trend. The proposed MPPT architecture takes only 9 ms to reach the reference with low overshoot and less voltage fluctuation in a steady state. whereas a single SEPIC converter requires 16 ms to track the voltage reference with voltage fluctuation between 465.87-475.75 V. Finally, at instant t=0.6 s, a step change of exhaust inlet temperature from 490 K to 745 K, and inlet mass flow from 47.5 g/s to 32.5 g/s is done. In terms of stability, response speed and accuracy, the advantage of the proposed MPPT architecture over the conventional single SEPIC converter is noted. Furthermore, a comparative study through the key figures is presented in Table 5.

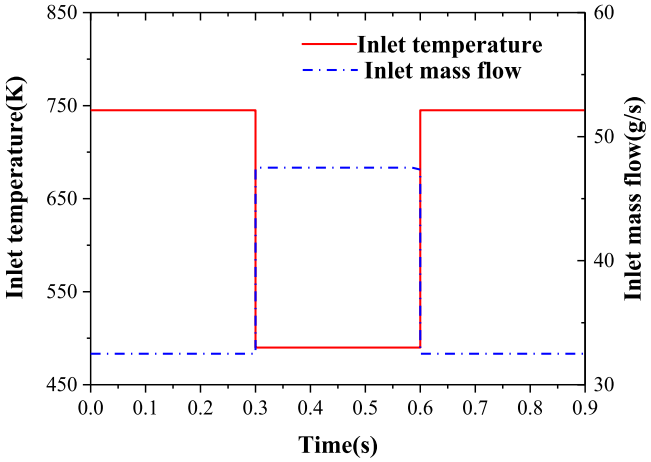

Fig. 13. Exhaust inlet temperature and mass flow profile.

5.2. System-level control discussion

In practice, Tianlong commercial vehicle usually travels on express highways for long-distance transportations. Moreover, it needs to carry cargoes for more than one hour without interruption, and the 765 s Highway Fuel Economy Test (HWFET) driving cycle is applied six times repetitively to 4590 s and it is used as the test driving cycle.

In order to accurately evaluate the performance of proposed energy harvesting strategy, the system model described in Fig. 15 is built in the MATLAB/Simulink environment. As a small battery is used for long-distance driving, the verification process of energy harvesting strategy is divided into two steps which the initial SOC of battery is 10%, 40%, and 70%, respectively. The specific setup of boundary conditions is listed in Table 6.

In this case we note the advantage of the proposed strategy over the other methods, in terms of simulation time as shown in Table 7.

Fig. 16 shows the simulation results under the modified HWFET driving cycle test, including the instantaneous output current of three SEPIC converters and the SOC of the battery, which can reflect the control performance of the proposed two-level energy harvesting strategy under three initial SOCs of the battery pack. As shown in Fig. 16(a) and (b), with low initial SOC, during the whole simulation period, the battery pack is charged fast to increase the SOC, while the AETEG is working in the MPPT mode to make efficient utilization of waste heat energy. Fig. 16(c) and (d) show that, with medium initial SOC, at the beginning the battery pack is charged as fast as possible within the normal SOC range, and the AETEG is working in the MPPT mode. However, the operation switches to the current mode when the SOC level exceeds the given threshold $\mathrm{SOC_{nom}}$ at about 2600 s. If the initial SOC is high, as in Fig. 16(e) and (f), the battery pack attempts to charge at a slower pace so the SOC of the battery can approach its upper limit. In this situation, the AETEG is always working in the current mode to reduce the power absorbed by the battery, when the SOC level is higher than $\mathrm{SOC_{nom}}$. Hence, the battery pack is always working at the optimal charging point to enhance the battery life.

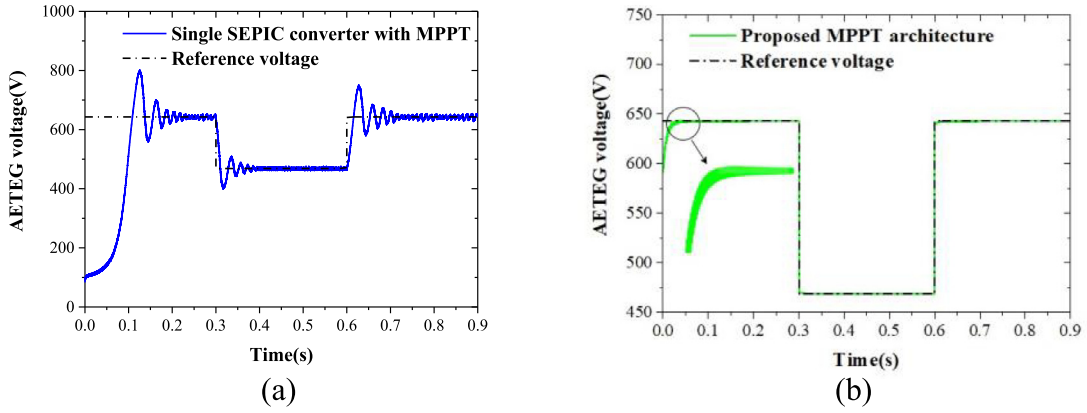

Fig. 14. (a) Automotive exhaust thermoelectric generator voltage response corresponding to single SEPIC converter with MPPT technique; (b) Automotive exhaust thermoelectric generator voltage response corresponding to proposed MPPT architecture.

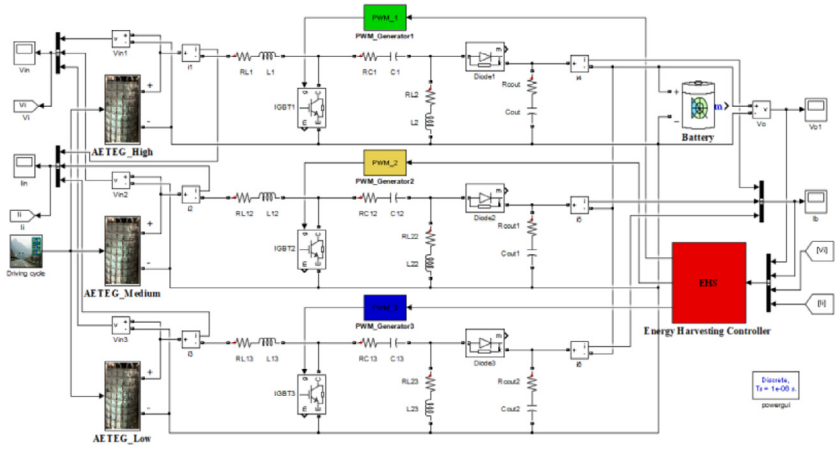

Fig. 15. Configuration of the distributed thermoelectric energy recovery system.

Table 5
Performance Comparison Using Different Architectures.

MPPT scheme	$t = 0$ s		$t = 0.3$ s		$t = 0.6$ s	
	Response time (s)	Overshoot (V)	Response time (s)	Overshoot (V)	Response time (s)	Overshoot (V)
Single SEPIC converter with MPPT	0.134	251.06	0.018	343.57	0.033	196.22
Proposed MPPT architecture	**0.06**	**0.62**	**0.009**	**1.01**	**0.005**	**1.31**

Table 6
Boundary conditions of the proposed energy harvesting strategy.

Parameter	Value	Parameter	Value
SOC_{min}	10%	I_{bmax}	30 A
SOC_{nom}	70%	P_H	450 W
SOC_{max}	90%	P_{batopt}	864 W
ΔSOC	0.006%	ΔP	1440 W

Table 7
Simulation time of the proposed strategy and other methods.

Algorithm	Time
EGMS	0.051 s
DP	0.109 s
PI	0.191 s
Hybrid strategy	0.076 s

The control performance of the distributed thermoelectric energy recovery system is presented in Table 8. The results show that the proposed two-level energy harvesting strategy can meet the power demand of the battery pack under different initial conditions. Moreover, it can be found that the two-level energy harvesting strategy can decrease the power loss of dc/dc converters and keep the battery pack working at the optimal point in the modified HWFET driving cycle.

In order to more intuitively reflect the advantages of system-level control, under the condition that the device-level control method remains unchanged, the traditional PI control strategy is adopted at the system level to achieve the comparison of system-level optimization effects. The energy harvesting strategy diagram based on classical PI control is shown in Fig. 17. The battery pack SOC is controlled by three PI regulators, and the output of the PI regulator is the DC/DC#1, DC/DC#2, DC/DC#3 reference output current, respectively.

In order to compare the average efficiency of the dc/dc converters of two strategies, this study calculated the efficiency of SEPIC converter according to (23). The average efficiency of three converters is expressed as

$$\eta_{con,avg} = \frac{1}{t}\int_0^t \left\{ I_b^* / \left(\frac{I_{o1}}{\eta_1} + \frac{I_{o2}}{\eta_2} + \frac{I_{o3}}{\eta_3} \right) \right\} dt \tag{34}$$

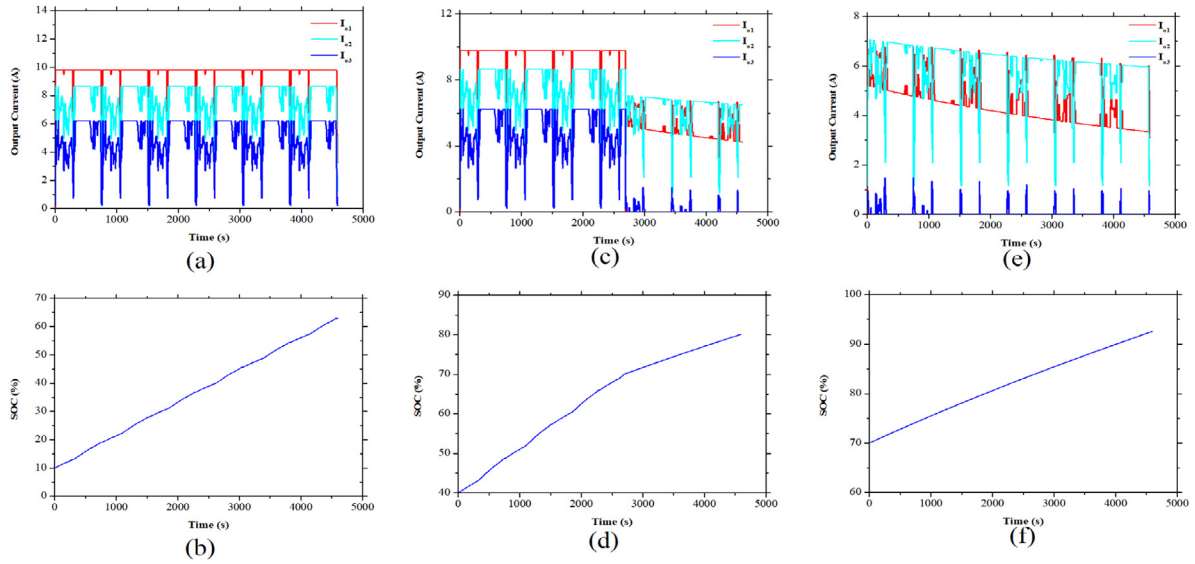

Fig. 16. (a) The simulation result of the two-level energy harvesting strategy (the initial SOC is 10%); (b) The charging curve of battery's SOC (the initial SOC is 10%); (c) The simulation result of the two-level energy harvesting strategy (the initial SOC is 40%); (d) The charging curve of battery's SOC (the initial SOC is 40%); (e) The simulation result of the two-level energy harvesting strategy (the initial SOC is 70%); (f) The charging curve of battery's SOC (the initial SOC is 70%).

Table 8
Control performance of the distributed thermoelectric energy recovery system based on two-level energy harvesting Strategy.

Performance	Initial SOC 10%	Initial SOC 40%	Initial SOC 70%
Average output current of DC/DC#1	9.59 A	7.74 A	4.48 A
Average output current of DC/DC#2	7.57 A	6.93 A	5.92 A
Average output current of DC/DC#3	5.06 A	2.95 A	0.05 A
SOC of battery pack	10% → 63.01%	40% → 80.11%	70% → 92.51%

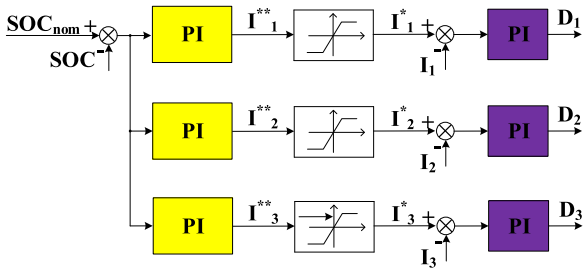

Fig. 17. Block diagram of the energy harvesting strategy based on PI control.

where, $\eta_{con,avg}$ is the average efficiency of three converters, and the converter efficiency η_1, η_2, and η_3 are obtained from (23). In addition, the charging energy of the battery is calculated as

$$E_{chg} = \int_0^t (P_{in1} \cdot \eta_1 + P_{in2} \cdot \eta_2 + P_{in3} \cdot \eta_3)\, dt \tag{35}$$

where, P_{in1}, P_{in2}, and P_{in3} are the output power of the high-, medium-, and low-temperature regions of the AETEG, respectively.

The performance of the proposed two-level energy harvesting strategy and the conventional PI-based control strategy are summarized and compared in Table 9.

From Table 9, regardless of the initial SOC level, it can be seen that the proposed two-level energy harvesting strategy is superior to the conventional PI control strategy in terms of energy conversion efficiency and charging energy.

Table 9
Control performance comparison using different strategies.

Initial SOC	$\eta_{con,avg}$		E_{chg}	
	PI	Two-level	PI	Two-level
10%	90.39%	92.79%	6553740 J	6727753 J
40%	92.15%	93.71%	4900493 J	4983454 J
70%	93.82%	94.19%	2863195 J	2874487 J

5.3. Two-level control discussion

To further confirm the capability of the proposed energy harvesting strategy, a Dongfeng Tianlong commercial vehicle platform is built, and a campus road test is designed. The performance of the AETEG/multi-string SEPIC converter/ $LiFePO_4$ battery pack system which is based on the proposed two-stage energy harvesting strategy is studied. Based on the proposed platform which includes AETEG, 51.2 V battery pack, recorder and DC power meter, the campus road test is performed to obtain the performance parameters of the thermoelectric power generation device. The overall system is shown in Fig. 18. Meanwhile, the SOCs of the battery pack, TEG's output power and voltage are measured and recorded every 30 s by Agilent 34792 A recorder. The parameters of vehicle are presented in Table 10.

After building the vehicle platform, the road test needs to be designed. Taking the requirements of long-distance high-speed driving into account, the modified HWFET driving cycle test is established in the previous chapters. Whereas, due to the modification, the vehicle with the exhaust gas recovery device cannot be tested on the highway.

Taking the safety requirements of high-speed driving into account, the HWFET driving cycle test is replaced by a campus road test. Because of the campus speed limit, the speed of vehicles

Fig. 18. Road test system.

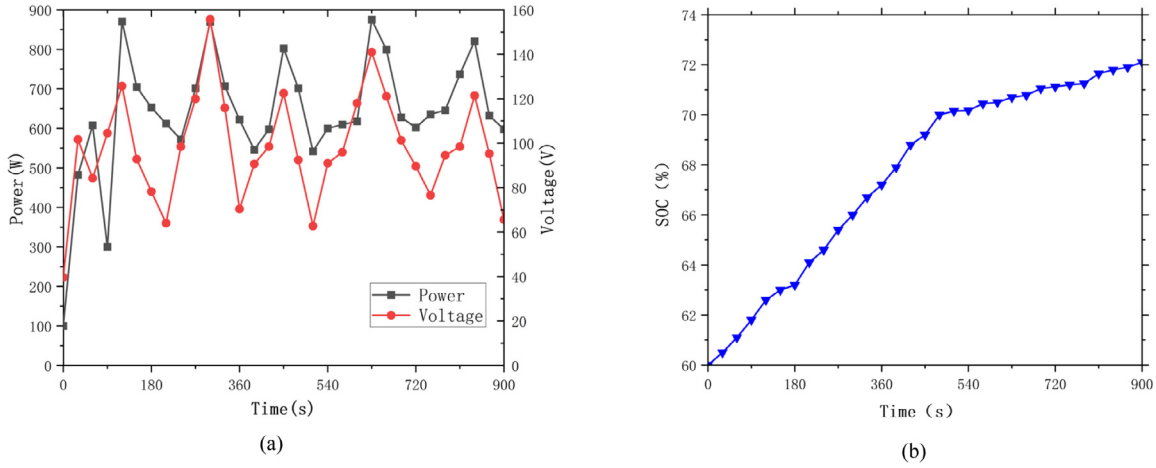

Fig. 19. Road test results. (a) Output power and voltage of automotive exhaust thermoelectric generator; (b) SOCs of $LiFePO_4$.

Table 10
Dongfeng Tianlong commercial vehicle parameters.

Name	Description	Value
Engine	Displacement (L)	11.12
	Rated power (kW)/Rotational speed (RPM)	30/1900
	Maximum torque (N m)/Rotational speed (RPM)	2000/1200–1400
Vehicle	Curb weight (kg)	8800
	Maximum gross mass (kg)	25000
	Dimensions (L · W · H, mm)	6810 × 2500×3030
	Wheelbase (mm)	3300
	Maximum speed (km/h)	98

on campus is limited to 10–40 km/h. In the campus road test, the car travels on a circular route with a total mileage of 7.5 kilometers. It takes about 15 min to complete the entire driving cycle.

Compared with the modified HWFET driving cycle, the campus road test has relatively less time and lower speed. It is impossible to get a complete SOC rising curve. In fact, according to the simulation results, the SOC curve under medium initial SOC can indicate the control capability of the proposed two-level energy harvesting strategy. For this reason, corresponding to the turning point in the simulation, the initial SOC is set as 60% to observe the transformation trend of SOC curve.

During the preparation process, $LiFePO_4$ needs to be charged to make its initial soc reach 60% and the car engine needs to be preheated, the heating time is set at 15 min.

Fig. 19(a) shows the changes in AETEG output power and voltage. The maximum power and maximum voltage of AETEG are 870.2 W and 154.1 V respectively in the whole test. However, due to the differences in speed and load between the actual test and modified HWFET simulation test, power and voltage in the simulation are higher than that of the road test. Fig. 19(b) presents the SOC change of the battery pack. With the initial SOC at 60%, the SOC level does not exceed the given threshold SOC_{nom}(70%) which makes the AETEG system run in MPPT mode. Under the control of proposed energy harvesting strategy, the battery pack is charged quickly to increase the SOC. Whereas, when the SOC exceeds the given threshold SOC_{nom} at about 480 s, the operation switches to the current mode, which makes battery pack charge at a slower rate compared with MPPT mode.

From 480 to 900 s, there is a slow increase from 70.04% to 72.12% in SOC. It shows that the proposed energy harvesting strategy helps the battery operate in current mode, which could prevent the battery from continuing to charge and enhance the life of $LiFePO_4$ battery pack. Therefore, no matter what the SOC of the battery is, the battery is always charged at the optimal rate to enhance battery life. Although the road test and the simulation

test run under different conditions, the road test results and the simulation results have similar SOC curves, which validate the feasibility of the proposed energy harvesting strategy.

6. Conclusions

In this paper, a distributed thermoelectric energy recovery system consisting of an eighteen-sided polygon prism shaped AETEG and a $LiFePO_4$ battery pack is developed. The AETEG is divided into three segments: the high-temperature region, the medium-temperature region, and the low-temperature region, while a multi-input single-output dc/dc converter with three SEPIC units are used to connect the three segments to the battery pack. The dynamic model of the system has been established and experimentally validated. A two-level energy harvesting strategy is next proposed for the distributed thermoelectric energy recovery system. The energy harvesting strategy contains the device control level and the system control level, and it is responsible for achieving the lowest loss of the dc/dc converters, keeping the battery working at the optimal point, and making full use of the AETEG waste heat. At the device control level, the AETEG is regulated by an MPPT-current dual-mode control algorithm, while the battery pack is regulated by droop control. At the system control level, the output current references of three SEPIC converters are calculated by a hybrid algorithm consisting of Equivalent generation maximizing strategy and Dynamic Programming. The proposed system and corresponding control strategy are verified by simulation under a modified HWFET driving cycle and a campus road test. Compared to the classical PI feedback control, the proposed two-level energy harvesting strategy can achieve high average efficiency of dc/dc converters (94.19%) when the initial SOC of battery is 70%. Therefore, the two-level energy harvesting strategy is more suitable for the distributed thermoelectric energy recovery system.

CRediT authorship contribution statement

Wenchao Zhu: Data curation, Investigation, Methodology, Writing – original draft. **Xiaolong Li:** Methodology, Software, Writing – original draft. **Yang Li:** Formal analysis, Investigation, Writing – review & editing. **Changjun Xie:** Conceptualization, Funding acquisition, Project administration, Supervision, Writing – review & editing. **Ying Shi:** Project administration, Validation.

Declaration of competing interest

The authors declare that they have no known competing financial interests or personal relationships that could have appeared to influence the work reported in this paper.

Acknowledgments

This research was supported by the National Natural Science Foundation of China (51977164), and the National Key Research and Development Program of China (2020YFB1506802).

References

Ali, Z.M., Vu Quynh, N., Dadfar, S., Nakamura, H., 2020. Variable step size perturb and observe MPPT controller by applying θ-modified krill herd algorithm-sliding mode controller under partially shaded conditions. J. Clean. Prod. 271, http://dx.doi.org/10.1016/j.jclepro.2020.122243.

Ashraf, M., Masoumi, N., 2016. A thermal energy harvesting power supply with an internal startup circuit for pacemakers. IEEE Trans. Very Large Scale Integ. (VLSI) Syst. 24, 26–37. http://dx.doi.org/10.1109/TVLSI.2015.2391442.

Carstens, J.H., Gühmann, C., 2015. Maximum power point controller for thermoelectric generators to support a vehicle power supply. Mater. Today: Proc. 790–803. http://dx.doi.org/10.1016/j.matpr.2015.05.099.

Crane, D., Lagrandeur, J., Jovovic, V., Ranalli, M., Adldinger, M., Poliquin, E., Dean, J., Kossakovski, D., Mazar, B., Maranville, C., 2013. TEG on-vehicle performance and model validation and what it means for further teg development. J. Electron. Mater. 42, 1582–1591. http://dx.doi.org/10.1007/s11664-012-2327-8.

Dalala, Z.M., Saadeh, O., Bdour, M., Zahid, Z.U., 2018. A new maximum power point tracking (MPPT) algorithm for thermoelectric generators with reduced voltage sensors count control. Energies 11, http://dx.doi.org/10.3390/en11071826.

Eakburanawat, J., Boonyaroonate, I., 2006. Development of a thermoelectric battery-charger with microcontroller-based maximum power point tracking technique. Appl. Energy 83, 687–704. http://dx.doi.org/10.1016/j.apenergy.2005.06.004.

Fang, W., Quan, S.H., Xie, C.J., Tang, X.F., Wang, L.L., Huang, L., 2016. Maximum power point tracking with dichotomy and gradient method for automobile exhaust thermoelectric generators. J. Electron. Mater. 45, 1613–1624. http://dx.doi.org/10.1007/s11664-015-4130-9.

Fernández-Yáñez, P., Gómez, A., García-Contreras, R., Armas, O., 2018. Evaluating thermoelectric modules in diesel exhaust systems: potential under urban and extra-urban driving conditions. J. Clean. Prod. 182, 1070–1079. http://dx.doi.org/10.1016/j.jclepro.2018.02.006.

Haidar, J.G., Ghojel, J.I., 2001. Waste heat recovery from the exhaust of low-power diesel engine using thermoelectric generators. In: Proceedings ICT2001. 20 International Conference on Thermoelectrics (Cat. No. 01TH8589). pp. 413–418. http://dx.doi.org/10.1109/ICT.2001.979919.

Hewawasam, L.S., Jayasena, A.S., Afnan, M.M.M., Ranasinghe, R.A.C.P., Wijewardane, M.A., 2020. Waste heat recovery from thermo-electric generators (TEGs). Energy Rep. 6, 474–479. http://dx.doi.org/10.1016/J.EGYR.2019.11.105.

Jaziri, N., Boughamoura, A., Müller, J., Mezghani, B., Tounsi, F., Ismail, M., 2020. A comprehensive review of thermoelectric generators: Technologies and common applications. Energy Rep. 6, 264–287. http://dx.doi.org/10.1016/J.EGYR.2019.12.011.

Karri, M.A., Thacher, E.F., Helenbrook, B.T., 2011. Exhaust energy conversion by thermoelectric generator: Two case studies. Energy Convers. Manage. 52, 1596–1611. http://dx.doi.org/10.1016/j.enconman.2010.10.013.

Kim, R.Y., Lai, J.S., 2008. A seamless mode transfer maximum power point tracking controller for thermoelectric generator applications. IEEE Trans. Power Electron. 23, 2310–2318. http://dx.doi.org/10.1109/TPEL.2008.2001904.

Kishita, Y., Ohishi, Y., Uwasu, M., Kuroda, M., Takeda, H., Hara, K., 2016. Evaluating the life cycle CO2 emissions and costs of thermoelectric generators for passenger automobiles: A scenario analysis. J. Clean. Prod. 126, 607–619. http://dx.doi.org/10.1016/j.jclepro.2016.02.121.

Li, X., Xie, C., Quan, S., Huang, L., Fang, W., 2018. Energy management strategy of thermoelectric generation for localized air conditioners in commercial vehicles based on 48, V electrical system. Appl. Energy 231, 887–900. http://dx.doi.org/10.1016/j.apenergy.2018.09.162.

Li, M., Xu, S., Chen, Q., Zheng, L.R., 2011. Thermoelectric-generator-based DC-DC conversion networks for automotive applications. J. Electron. Mater. 113, 6–1143. http://dx.doi.org/10.1007/s11664-011-1557-5.

Liu, Y.H., Chiu, Y.H., Huang, J.W., Wang, S.C., 2016. A novel maximum power point tracker for thermoelectric generation system. Renew. Energy 97, 306–318. http://dx.doi.org/10.1016/j.renene.2016.05.001.

Liu, X., Deng, Y.D., Li, Z., Su, C.Q., 2015. Performance analysis of a waste heat recovery thermoelectric generation system for automotive application. Energy Convers. Manage. 90, 121–127. http://dx.doi.org/10.1016/j.enconman.2014.11.015.

Liu, C., Liu, L., 2020. The global peak forecasting method for PV array based on the conservation of energy at uniform and partial shading. Energy Rep. 6, 113–122. http://dx.doi.org/10.1016/J.EGYR.2020.12.002.

Mao, M., Cui, L., Zhang, Q., Guo, K., Zhou, L., Huang, H., 2020. Classification and summarization of solar photovoltaic MPPT techniques: A review based on traditional and intelligent control strategies. Energy Rep. 6, 1312–1327. http://dx.doi.org/10.1016/J.EGYR.2020.05.013.

Montecucco, A., Knox, A.R., 2015. Maximum power point tracking converter based on the open-circuit voltage method for thermoelectric generators. IEEE Trans. Power Electron. 30, 828–839. http://dx.doi.org/10.1109/TPEL.2014.2313294.

Nagayoshi, H., Nakabayashi, T., Maiwa, H., Kajikawa, T., 2011. Development of 100-W high-efficiency MPPT power conditioner and evaluation of TEG system with battery load. J. Electron. Mater. 65, 7–661. http://dx.doi.org/10.1007/s11664-010-1499-3.

Park, J., do, Lee, H., Bond, M., 2014. Uninterrupted thermoelectric energy harvesting using temperature-sensor- based maximum power point tracking system. Energy Convers. Manage. 86, 233–240. http://dx.doi.org/10.1016/j.enconman.2014.05.027.

Park, H., Sim, M., Kim, S., 2015. Achieving maximum power from thermoelectric generators with maximum-power-point-tracking circuits composed of a boost-cascaded-with-buck converter. J. Electron. Mater. 44, 1948–1956. http://dx.doi.org/10.1007/s11664-014-3606-3.

Sun, K., Wu, H., Cai, Y., Xing, Y., 2014. A power conditioning stage based on analog-circuit MPPT control and a superbuck converter for thermoelectric generators in spacecraft power systems. J. Electron. Mater. 43, 2287–2292. http://dx.doi.org/10.1007/s11664-014-3045-1.

Twaha, S., Zhu, J., Maraaba, L., Huang, K., Li, B., Yan, Y., 2017a. Maximum power point tracking control of a thermoelectric generation system using the extremum seeking control method. Energies 10, http://dx.doi.org/10.3390/en10122016.

Twaha, S., Zhu, J., Yan, Y., Li, B., Huang, K., 2017b. Performance analysis of thermoelectric generator using dc-dc converter with incremental conductance based maximum power point tracking. Energy Sustain. Dev. 37, 86–98. http://dx.doi.org/10.1016/j.esd.2017.01.003.

Wu, H., Sun, K., Chen, M., Chen, Z., Xing, Y., 2013a. Hybrid centralized-distributed power conditioning system for thermoelectric generator with high energy efficiency. In: 2013 IEEE Energy Conversion Congress and Exposition. ECCE 2013, pp. 4659–4664. http://dx.doi.org/10.1109/ECCE.2013.6647325.

Wu, H., Sun, K., Chen, M., Xing, Y., 2014. Evaluation of power conditioning architectures for energy production enhancement in thermoelectric generator systems. J. Electron. Mater. 43, 1567–1573. http://dx.doi.org/10.1007/s11664-013-2795-5.

Wu, H., Sun, K., Zhang, J., Xing, Y., 2013b. A TEG efficiency booster with buck-boost conversion. J. Electron. Mater. 42, 1737–1744. http://dx.doi.org/10.1007/s11664-012-2407-9.

Yang, B., Zhang, M., Zhang, X., Wang, J., Shu, H., Li, S., He, T., Yang, L., Yu, T., 2020. Fast atom search optimization based MPPT design of centralized thermoelectric generation system under heterogeneous temperature difference. J. Clean. Prod. 248, http://dx.doi.org/10.1016/j.jclepro.2019.119301.

Yang, B., Zhong, L., Zhang, X., Shu, H., Yu, T., Li, H., Jiang, L., Sun, L., 2019. Novel bio-inspired memetic salp swarm algorithm and application to MPPT for PV systems considering partial shading condition. J. Clean. Prod. 215, 1203–1222. http://dx.doi.org/10.1016/j.jclepro.2019.01.150.

Yu, C., Chau, K.T., 2009. Thermoelectric automotive waste heat energy recovery using maximum power point tracking. Energy Convers. Manage. 50, 1506–1512. http://dx.doi.org/10.1016/j.enconman.2009.02.015.

Zhang, B., Chen, Y., Wang, Z., Shakibi, H., 2020. Thermodynamic, environmental, and optimization of a new power generation system driven by a gas turbine cycle. Energy Rep. 6, 2531–2548. http://dx.doi.org/10.1016/J.EGYR.2020.09.003.